Research Square

Preprints are preliminary reports that have not undergone peer review.
They should not be considered conclusive, used to inform clinical practice,
or referenced by the media as validated information.

Nonlinear symmetry-driven circular polarization purification for sub-femtosecond-scale hologram switching

Dmitry Pidgayko

pidgai03@gmail.com

Friedrich Schiller University Jena, Institute of Applied Physics, Abbe Center of Photonics
https://orcid.org/0000-0002-5485-2968

Shiu Hei Lam

Friedrich Schiller University Jena, Institute of Applied Physics, Abbe Center of Photonics

Benjamin Laudert

Friedrich Schiller University Jena https://orcid.org/0009-0001-7411-6570

Maximilian Weissflog

Friedrich Schiller University Jena https://orcid.org/0000-0002-3091-1441

Duk-Yong Choi

The Australian National University https://orcid.org/0000-0002-5339-3085

Falk Eilenberger

Friedrich-Schiller-Universität, Jena https://orcid.org/0000-0002-4646-2484

Thomas Pertsch

Friedrich Schiller University Jena https://orcid.org/0000-0003-4889-0869

Isabelle Staude

Friedrich Schiller University https://orcid.org/0000-0001-8021-572X

Article

Keywords:

Posted Date: November 26th, 2026

DOI: https://doi.org/10.21203/rs.3.rs-11469627/v1

License: This work is licensed under a Creative Commons Attribution 4.0 International License.
Read Full License

Additional Declarations: There is **NO** Competing Interest.

Nonlinear symmetry-driven circular polarization purification for sub-femtosecond-scale hologram switching

Dmitry Pidgayko[1,2*], Shiu Hei Lam[1], Benjamin Laudert[2], Maximilian Weissflog[1], Duk-Yong Choi[3], Falk Eilenberger[1,2,4], Thomas Pertsch[1,2,4], Isabelle Staude[1,2]

[1]Institute of Applied Physics, Abbe Center of Photonics, Friedrich Schiller University Jena, Jena, Germany.
[2*]Institute of Solid State Physics, Friedrich Schiller University Jena, Jena, Germany.
[3]Laser Physics Centre, Research School of Physics, Australian National University, Canberra, Australia.
[4]Fraunhofer Institute for Applied Optics and Precision Engineering IOF, Jena, Germany.

*Corresponding author(s). E-mail(s): pidgai03@gmail.com;

Abstract

We report sub-femtosecond-scale hologram switching enabled by a nonlinear, symmetry-protected circular polarization purification effect based on second-harmonic generation in 3R-TMD. Two orthogonally polarized pump pulses with a tunable inter-pulse delay $\boldsymbol{\tau_D}$, aligned along the armchair and zig-zag axes of a thick 3R-MoS_2 crystal, generate second harmonic signal whose degree of circular polarization $\boldsymbol{\sigma^{(2\omega)}}$ is protected by the $\boldsymbol{\chi^{(2)}}$ tensor symmetry against small deviations from exact pump circularity. This yields stable plateaus of pure left- and right-handed SHG polarization within delay windows τ_{LH} and τ_{RH}, governed by a general transfer relation $|\boldsymbol{\sigma^{(2\omega)}}| \geq |\boldsymbol{\sigma^{(\omega)}}|$ that holds independently of the excitation scheme. Illuminating a Pancharatnam–Berry phase metasurface with this purified signal yields robust, high-contrast holographic switching: cross-correlation analysis reveals alternating plateaus (zero-normalized cross-correlation $\approx \mathbf{0.9}$), with channel transitions confined to under one femtosecond, while high-fidelity switching persists over delays as large as $\pm\mathbf{140}$ fs, comparable to the pump pulse duration.

Introduction

In recent years, two-dimensional transition metal dichalcogenides (TMDs) have emerged at the forefront of nanophotonics due to their exceptional electronic and optical properties [1]. Driven by direct-bandgap nature and strong Coulomb interaction, monolayer TMDs exhibit rich exciton physics and enhanced photoluminescence [2]. The broken inversion symmetry of the single-layer lattice, characterized by the D_{3h} point group [3], induces robust spin-valley locking and dictates a strong second-order optical nonlinearity [4]. The second-order optical susceptibility of two-dimensional TMDs reaches an exceptionally high value of $|\chi^{(2)}| \approx 100 - 1000$ pm/V [5], facilitating pronounced three-wave mixing phenomena such as second-harmonic generation (SHG), spontaneous parametric down-conversion, and sum- and difference-frequency generation [6, 7]. However, the atomically thin nature of the monolayer negates the generation efficiency, which scales with thickness L as $\eta_{\mathrm{SHG}} = I_{2\omega}/I_{\omega} \propto |\chi^{(2)}|L^2$ [8].

The multilayer rhombohedral 3R-TMD phase with non-centrosymmetric stacking bypasses this bottleneck. The 3R-TMD crystal lattice features C_{3v} symmetry with a three-fold rotational axis and mirror planes [9]. This yields the same in-plane second-order susceptibility tensor components as in the monolayer [9, 10]. The magnitude of $|\chi^{(2)}|$ reaches a substantial 400 pm/V [11], while the crystal thickness has ranged from tens to hundreds of nanometers across various studies [9, 12, 13]. Finally, the high refractive index facilitates the realization of resonant nanoparticles and quasi-BIC metasurfaces, further enhancing the SHG efficiency [10, 12, 14, 15].

In both monolayer TMD and multilayer 3R-TMDs, the symmetry of the $\chi^{(2)}$ tensor determines the polarization dynamics of second-order nonlinear processes. For instance, the three-fold rotational symmetry in 3R-TMD-based spontaneous parametric down-conversion guarantees the generation of maximally entangled polarization Bell states [9]. Likewise, Klimmer et al. [16] leveraged the tensor symmetry of monolayer MoS_2 to demonstrate delay-dependent amplitude and polarization modulation of the SH signal generated with two orthogonally polarized pump pulses. This approach was later utilized in a study by Sinelnik et al. in combination with Pancharatnam–Berry (PB) phase metasurfaces [17]. Depending on the optical delay - either exceeding the pulse duration or fully synchronized - the metasurfaces yielded different functional responses to allow for femtosecond-scaled second-harmonic wavefront control. However, the complexity of the wavefronts demonstrated so far remained confined to beam deflection and vortex beam switching. This is mainly due to the limited SHG conversion efficiency of the TMD monolayers, which critically reduces the signal-to-noise ratio if the generated SHG beam is expanded to interact with more complex spatially variant metasurfaces. Moreover, the desired switching functionality was previously based on two distinct regimes: fully synchronized beams with zero delay or temporally non-overlapping pulses with a delay exceeding the pulse duration, whereas intermediate regimes with ultrashort delay at sub-femtosecond scale resolution have not been thoroughly investigated.

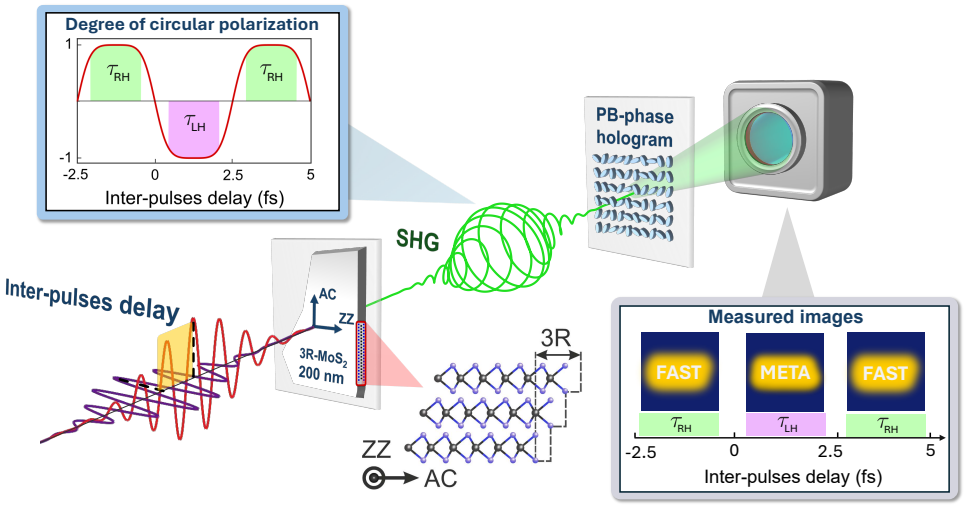


Fig. 1 Concept of the circular polarization purification for hologram switching. Two orthogonally polarized pump pulses with an inter-pulse delay τ_D propagate through a thick 3R-MoS_2 layer, generating SH signal. The degree of circular polarization (DOCP) of the SHG is controlled by τ_D, locking into pure LCP and RCP states within the time intervals τ_{LH} and τ_{RH}. Subsequent illumination of a Pancharatnam–Berry phase metasurface yields stable holographic reconstructions throughout the τ_{LH} and τ_{RH} delay regimes, with sharp switching between channels.

Here we advance this approach along two main directions, directly addressing the aforementioned challenges. First, we switch to 3R-TMD to boost the SHG efficiency. Second, we carry out in-depth investigation of the SHG polarization emerging at *sub-pulse* delay times between the illumination pulses, at sub-femtosecond timescales. In our scheme, we use two orthogonally polarized pump pulses aligned along armchair (AC) and zig-zag (ZZ) axes of the 3R-MoS_2 crystal (see Fig. 1). Both pump pulses are identical in duration and frequency, with a tunable inter-pulse delay τ_D. In studies with a similar second-harmonic generation geometry and time delays comparable to or much shorter than the pulse duration [15–18], the observed effects are commonly referred to as "ultrafast". This can be misleading, since $\chi^{(2)}$ is conventionally assumed to respond instantaneously to the optical excitation — an approximation valid when the driving frequencies lie far from any material resonance [19]. Therefore, in this paper, we prefer the term "ultrashort" delay. On a sub-cycle timescale with ultrashort delays, varying τ_D modulates the ellipticity of the pump polarization, formed by the superposition of the two pulses, from linear to pure circular (RCP or LCP). As previously shown [16], at near-zero delays corresponding to an equivalent phase difference of $\pm\pi/2$, the SHG possesses either right- or left-circular polarization. The effect is fully dictated by the material symmetry and the structure of its $\chi^{(2)}$ tensor. Here, we show that pure circular polarization in the SH is maintained not merely at isolated τ_D points, but sustained over an extended delay range. It is manifested as plateau-like

features in the SHG degree of circular polarization (upper panel in Fig. 1). We find that this behavior originates from a symmetry-protected purification mechanism: the C_{3v} point-group symmetry of the crystal renders the second-harmonic circular polarization inherently purer than that of the pump, suppressing residual pump ellipticity, irrespective of the excitation scheme. Combining this effect with a high SHG efficiency, we demonstrate delay-dependent hologram switching on a sub-femtosecond timescale using a PB-phase metasurface. The ultrashort sub-femtosecond scale of this effect provides a versatile route toward maximizing the spatio-temporal information density within structured optical fields, while the symmetry of the $\chi^{(2)}$ tensor enables direct encoding into distinct RCP and LCP states. Finally, the purification effect provides robustness against delay fluctuations in the pump. Therefore such a system holds great potential for advancing optical communication technologies through direct information encoding into a circular polarization basis with enhanced delay and phase jitter tolerance.

Symmetry-driven circular polarization purification

The nonlinear symmetry-driven circular polarization purification in a double-pulse excitation geometry can be illustrated with a simplified model of two monochromatic plane waves. Here we treat the 3R-TMD crystal as a two-dimensional nonlinear film of uniform thickness, with its ZZ and AC crystallographic axes oriented along the $\hat{\boldsymbol{x}}$- and $\hat{\boldsymbol{y}}$-directions, respectively. Assuming normal incidence, $E_z = 0$, and C_{3v} point-group symmetry, SHG is driven by $\chi^{(2)}_{yyy} = -\chi^{(2)}_{yxx} = -\chi^{(2)}_{xxy} = -\chi^{(2)}_{xyx} = \chi^{(2)}$ second-order susceptibility components [19]. Then, the second-harmonic electric fields are proportional to [20, 21]:

$$\begin{cases} E_x^{(2\omega)} \propto 2\chi^{(2)} E_x E_y \\ E_y^{(2\omega)} \propto \chi^{(2)}(E_x^2 - E_y^2) \end{cases} . \tag{1}$$

Let two monochromatic plane waves of identical frequency ω_0 and amplitude E_0, linearly polarized along the $\hat{\boldsymbol{x}}$ and $\hat{\boldsymbol{y}}$ axes, with a phase difference φ, serve as the pump. The phase difference can be related to the inter-pulse time delay as $\varphi = \omega_0 \tau_D$, where ω_0 is the central frequency and τ_D is the delay between the two pulses. Evidently, the phase φ controls the polarization state of the resulting field. We quantify this state by the degree of circular polarization (DOCP), defined as $\sigma = 2\,\mathrm{Im}\{E_x^* E_y\}/|\mathbf{E}|^2$ [22–25]. The corresponding total electric field of the pump and its DOCP are:

$$\mathbf{E} = E_0(\hat{\boldsymbol{x}} + e^{i\varphi}\hat{\boldsymbol{y}})e^{ikz},\ \sigma^{(\omega)} = \sin\varphi. \tag{2}$$

Direct substitution into Eq. 1 yields expressions for the second-harmonic far-field amplitude and its DOCP:

$$\mathbf{E}^{(2\omega)} \propto \hat{\boldsymbol{x}} - i\sin\varphi\hat{\boldsymbol{y}},\ \sigma^{(2\omega)} = -\frac{2\sin\varphi}{1+\sin^2\varphi} \tag{3}$$

Figure 2a compares $\sigma^{(2\omega)}(\varphi)$ and $-\sigma^{(\omega)}(\varphi)$ as functions of the phase delay. Here it is seen that the absolute value of the DOCP in the SH is almost always higher than in the

fundamental. In the Supplementary Information, we show that in the vicinity of the phases $\pm\pi/2$ the small ellipticity of the excitation is suppressed in second harmonic, resulting in a stabilization of $\sigma^{(2\omega)}$. Thus, owing to the 3R-TMD crystal symmetry, the second-harmonic DOCP is stabilized at its extremal values ± 1, which we refer to as circular polarization purification.

It can be noticed that the DOCP of the pump and of the second harmonic are related by:

$$\sigma^{(2\omega)} = -\frac{2\,\sigma^{(\omega)}}{1+\left(\sigma^{(\omega)}\right)^2}\,. \tag{4}$$

This result follows in full generality from the second-harmonic fields dictated by the symmetry of the $\chi^{(2)}$ tensor (see Supplementary Information). Figure 2b explicitly shows that the second-harmonic DOCP always lies in the region $\left|\sigma^{(2\omega)}\right| \geq \left|\sigma^{(\omega)}\right|$, with equality at $\sigma^{(\omega)} = 0$ and $\sigma^{(\omega)} = \pm 1$. The second harmonic is thus never less circularly polarized than the excitation that generates it, independently of the excitation scheme. That constitutes a general nonlinear symmetry-protected circular polarization purification.

Under pulsed-pump experimental conditions, the excitation amplitudes are temporally modulated. Assuming the temporal envelope varies slowly compared to a single optical cycle, each beam can be considered quasi-monochromatic [20]. Ideal circular polarization in the pump arises only when both pulses possess approximately equal amplitudes, which holds true at small inter-pulse delays. Treating the system via two monochromatic plane waves therefore remains a valid approximation for inter-pulse delays spanning a few pump field oscillations. As the delay increases, the temporal overlap region with balanced amplitudes narrows, thereby reducing the average degree of circularity of the overall pump pulse. Nonetheless, the 3R-TMD crystal maintains a high degree of circular polarization over a delay range comparable to the pump pulse duration, as confirmed by our further experimental observations.

1 Samples characterization

1.1 SHG mapping of 3R-MoS_2 sample

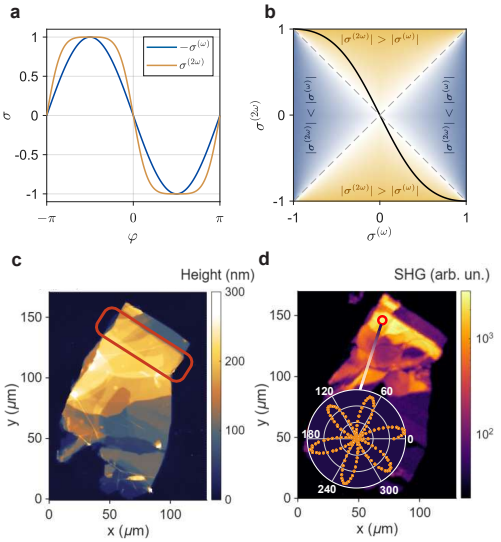


Fig. 2 (a) DOCP of the SH and the pump comparison vs phase delay. (b) General circular polarization purification. Black solid line represents relation (4). (c) 3R-MoS_2 sample thickness map. (d) SHG intensity distribution map on a logarithmic scale. Inset: polarization-resolved SHG intensity, measured from the region enclosed by the red circle.

The SHG intensity in 3R-TMD is governed by its physical thickness. As the latter increases, optical propagation and phase-matching effects begin to play a decisive role [19]. The overall second-harmonic intensity increases until reaching the coherence length, beyond which it decays due to destructive interference [8, 19, 26]. Following the approach in [8, 9], we established the thickness dependence of the SHG efficiency for 3R-MoS_2 at 1500 nm revealing the optimal thickness of the crystal at 195 nm. The discrepancy in reported refractive index values must be taken into account, as they range from 3.9 to 4.1 at 1500 nm, and from 4.5 to 4.8 at 750 nm across different studies [8, 14, 27]. Based on these data, the first SHG intensity maximum is expected at a thickness in the range of 180–195 nm. Accordingly, we chose a sample containing uniform regions with thicknesses inside this target range. The geometric profile of the selected sample (see Fig. 2c) was measured using vertical scanning interferometry (VSI, Bruker Contour GT-K). The sample exhibits regions of varying thickness, including the target range (inside the red rectangle in Fig. 2c). Next, we acquired the spatial distribution of the SHG intensity shown in Fig. 2d on a logarithmic scale (see Methods for measurement details). For the region with the maximum SHG intensity (red circle in Fig. 2d), we carried out classical polarization-resolved SHG measurements (see Methods) [9, 21, 28, 29]. As expected, we measured the characteristic six-lobed pattern

shown in the inset of Fig. 2d, which confirms the three-fold symmetry of the crystal in the area of interest [26]. Having validated both its high generation efficiency and structural symmetry, we utilized this position on the sample for the main nonlinear holographic switching measurements.

1.2 Polarization-dependent holographic projection with a phase-modulating metasurface

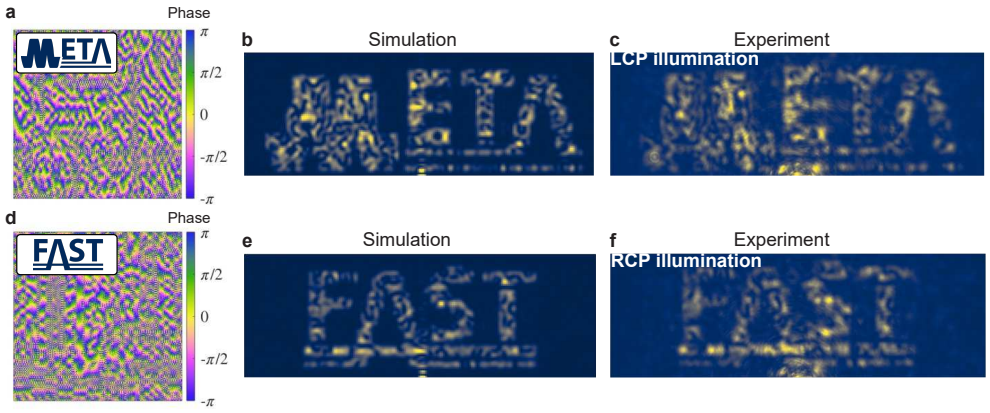


Fig. 3 Design, simulation and characterization of the polarization-dependent phase-modulating metasurface. (a),(d) Phase distribution maps for LCP and RCP holographic channels. The insets present the regions of the "META" and "FAST" logos in target images used to generate the phase distributions. (b), (e) Simulated holographic projections under the LCP and the RCP incident light, respectively. (c), (f) Measured holographic projections under the LCP and the RCP incident light, respectively.

The switching of holographic projection was achieved using a polarization-dependent metasurface which encodes individual holographic phase masks in its RCP and LCP channels. As a demonstration, we designed holographic phase masks to project the icons "META" (Fig. 3a) and "FAST" (Fig. 3d) in the back-focal plane for the LCP channel and RCP channel, respectively. The phase masks were computer-generated using the iterative Fourier transform algorithm [30, 31], considering a plane wave incidence with periodic boundary conditions. Details of the phase mask design are provided in the supplementary information. The phase-mask-encoding metasurface consists of an array of amorphous silicon nanoposts of varying dimensions across a silica substrate. Based on the local periodic approximation, propagation phases and Pancharatnam–Berry phases of the nanoposts were utilized to provide two degrees of freedom for independent phase modulation in the LCP and RCP channels [17, 32]. To employ the Pancharatnam–Berry phase of the cross-polarization transmission for phase modulation, a library of nanoposts with minimum co-polarization transmission was selected. The propagation phases of the nanoposts in the library vary according

to their different dimensions. The nanoposts were arranged spatially on the substrate by mapping the phases of their cross-polarization transmission to the designed holographic phase masks in the LCP and RCP channels[17].

To simulate the holograms expected experimentally, the pump was assumed to be a paraxial Gaussian beam [33] characterized in the sample plane by its central offset (x_0, y_0) and a beam waist w. In the model, the phase masks shown in Figs. 3(a) and 3(d) were first multiplied by a Gaussian amplitude profile aligned at their center, with a beam waist matching the effective dimensions of the metasurface (see additional scripts in supplementary information). Subsequently, the complex field was propagated to the far field, resulting in a holographic projection in the back-focal plane presented in Figs. 3b and 3e with LCP and RCP incident light, respectively. The simulated patterns clearly exhibit the features of the target "META" and "FAST" images, along with a typical speckle structure arising from the finite size of the phase-modulating metasurface.

Following the metasurface fabrication, the metasurfaces were pre-characterized using a back-focal-plane imaging technique (see Methods). The selected metasurface was illuminated at a wavelength of 750 nm under LCP and RCP incident light, with the corresponding results shown in Figs. 3c and 3f, respectively. To quantify the agreement between simulation and experimental results, we employ the zero-normalized cross-correlation (ZNCC) defined as [34, 35]:

$$\mathrm{ZNCC}(S,E) = \frac{\sum_{i,j}\left(S_{ij}-\overline{S}\right)\left(E_{ij}-\overline{E}\right)}{\sqrt{\sum_{i,j}\left(S_{ij}-\overline{S}\right)^2\sum_{ij}\left(E_{ij}-\overline{E}\right)^2}}, \tag{5}$$

where S and E are simulated and experimental images being compared (represented by real-valued matrices S_{ij} and E_{ij}, and i, j for the pixel indices), $\overline{S}$ and $\overline{E}$ are their respective mean intensities over all matrix elements. The ZNCC takes values in the range $[-1, 1]$, where 1 indicates perfect similarity, 0 represents a complete absence of correlation, and -1 denotes anti-correlation. Prior to calculating the ZNCC, it should be noted that in the experiment the position and size of the focused pump spot were adjusted to achieve the best result rather than set based on geometric centering considerations. Therefore, the ZNCC value itself was calculated using an optimization algorithm (see Supplementary Information) where the parameters x_0, y_0 and w – identical for both holograms – of the modeled Gaussian pump and the simulated holograms were optimized to maximize the correlation. The optimization yielded high ZNCC values of 0.85 for the "META" holographic channel and 0.86 for the "FAST" channel. Given that the practical fidelity threshold in correlation analysis is typically set to ZNCC ≥ 0.8 [36–38], the reconstructed holograms under RCP and LCP excitation demonstrate good agreement with numerical simulations within this regime. The discrepancy from unity reflects the combined effect of distortions in the non-Gaussian pump beam profile, non-ideality of the quarter-wave plate, and minor fabrication defects in the metasurface. Nonetheless, our results indicate that under circular polarization at 750 nm both encoded holographic channels can be unambiguously identified.

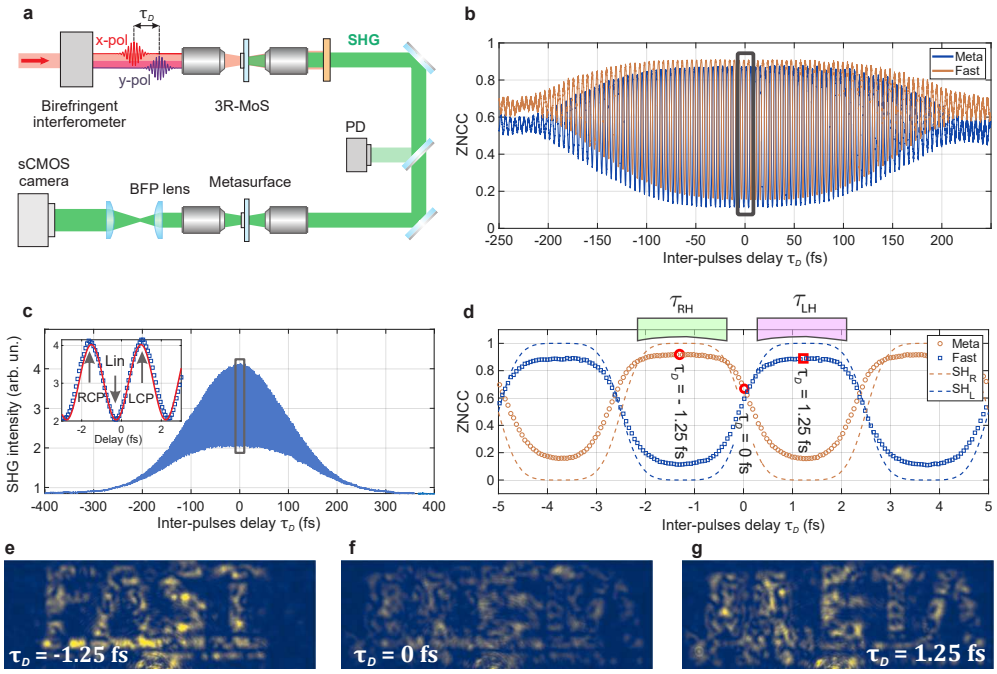


Fig. 4 Experimental demonstration of delay-dependent polarization switching. (a) Layout of the experimental setup. (b) ZNCC traces for both holographic channels calculated for holograms taken over the delay range of [-250, 250] fs. (c) SHG intensity dependence on the delay. Inset: Zoomed-in SHG intensity for [-2.5, 2.5] fs. The red curve represents theoretical $I^{(SHG)} \propto 1 + \sin^2(\omega_0 \tau_D + \varphi_0)$. (d) Zoomed-in ZNCC traces. SH_L and SH_R are the decomposition coefficients of the total second-harmonic intensity into its left- and right-circular components, respectively. (e)-(g) Measured holograms with the respective delays.

Sub-femtosecond hologram switching

In light of the presented concepts, we utilize the nonlinear delay-dependent circular polarization purification to achieve sub-femtosecond hologram switching. A schematic of the experimental setup is presented in Fig. 4a. The pump at a central wavelength of 1500 nm passes through a birefringent interferometer (Nireos Gemini), which splits the beam into orthogonal x- and y-polarized components (aligned with the AC and ZZ axes of the 3R-MoS_2 sample) and also serves as a fine delay line. The delay between the two beams is precisely controlled over a broad temporal range with a resolution higher than 0.1 fs. Upon passing through the 3R-MoS_2 crystal (characterized in Section 3.1), the SHG can be guided either to a photodetector (Nireos Spider) channel for SHG intensity measurement, or to a main channel containing the metasurface (characterized in Section 3.2). The generated holograms are imaged onto an sCMOS camera (Teledyne Prime 95B) using a back-focal-plane lens system. First, we examine the SHG intensity as a function of the inter-pulse delay τ_D (see Fig. 4c), which is in excellent agreement with earlier reports [15, 16]. At a near-zero delay, the SHG intensity dynamics closely follow $I^{(SHG)} \propto 1 + \sin^2(\omega_0 \tau_D + \varphi_0)$ derived from Eq. (1) (red line in inset Fig. 4c).

The initial phase φ_0 is tied to the interferometer calibration. The local minima at $\tau_D \approx 0$ correspond to linearly polarized SHG, whereas the maxima represent RCP and LCP states. At large delays, the intensity drops by approximately a factor of four relative to the RCP/LCP peak, as expected: in this regime, the two pump pulses do not overlap in the time domain and generate SH signal independently. Each beam then contributes only through the second term in Eq. (1), as it possesses a single electric field component, in contrast to the first term in Eq. (1), which governs the RCP/LCP state.

The nonlinear circular polarization purification is not directly resolved in the SHG intensity trace. We reveal this effect by recording holographic images from the metasurface across the inter-pulse delay range of $[-250, 250]$ fs. To this end, the photodetector channel was bypassed, ensuring that the unsplit SHG signal entirely propagated through the metasurface channel. The complete set of the captured holograms for each $\tau_D \in [-250, 250]$ fs is provided in the Supplementary Information. Here, we focus on some specific delays (see Figs. 4e–g). At $\tau_D = -1.25$ fs, the reconstructed image in Fig. 4e clearly reproduces the "FAST" pattern shown in Fig. 3f, taken under single-pulse RCP illumination. Similarly, the image in Fig. 4g captured at $\tau_D = 1.25$ fs is consistent with Fig. 3c. At the intermediate delay of 0 fs (Fig. 4f), a combination of both images is barely recognizable. Based on measurements at $\tau_D = -1.25$ fs and $\tau_D = 1.25$ fs (Figs. 4e and 4g), we prepared simulated holographic projections of the "FAST" and "META" patterns, which served as reference masks for computing the correlation with the measured image at every delay. For all experimental images, we calculated a pair of correlations against these two reference masks, thereby obtaining the delay-dependent decomposition into holographic channels shown in Fig. 4b.

We first examine the experimental results within the delay window of ± 5 fs. In this range, the zoomed-in cross-correlation traces in Fig. 4d exhibit alternating plateau-like regions peaking near 0.9. For comparison with theory, it is convenient here to introduce the decomposition coefficients of the total second-harmonic intensity into its left- and right-circular components (see Supplementary information), shown as dashed SH_R and SH_L curves. We note the excellent agreement between the correlation values and the circular-component contributions obtained for the simplified monochromatic-pump model. The experimental ZNCC values rise from 0.85–0.86 during single-pulse pre-characterization to 0.9 and above in the delay-controlled scheme, further indicating the circular polarization purification effect. Further, we estimate the stability window of the holographic channels. According to the practical threshold of ZNCC ≥ 0.8 discussed above, the effective delay ranges τ_{LH} and τ_{RH} are estimated to span approximately 1.7 fs, over which the hologram projection exhibits high robustness against delay fluctuations. Meanwhile, the transition between holographic channels takes place within a shorter delay window not exceeding one femtosecond. This behavior therefore constitutes hologram switching rather than reconfiguration: although the evolution is formally continuous in τ_D, it proceeds in a step-like manner between two highly stable states.

Anchored by the operational threshold of ZNCC ≥ 0.8, the global envelope of the correlation traces for both channels sustains values above this level across a broad delay range of $-140 < \tau_D < 140$ fs. A detailed examination of the interval from -140

to −130 fs reveals that the plateau features are no longer observed (see Fig. 5a). Nevertheless, high correlation values of ZNCC ≥ 0.8 are successfully attained. The remarkable nature of this result becomes evident when examining the SHG intensity in Fig. 4c. At delays of around −140 fs, the local SHG peaks barely reach half of their maximum intensity, indicating a weak temporal overlap of the pump pulses. Despite this low field overlap, the average circularity of the SHG remains high enough to ensure clear holographic image reconstruction. Thus, symmetry-protected polarization purification persists well beyond the plateau regime itself, enabling robust hologram channel identification across the full delay range comparable to the pump pulse duration.

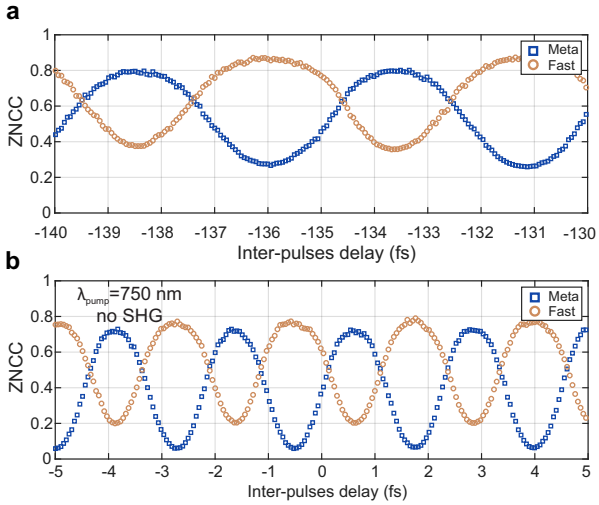


Fig. 5 **a**, Zoomed-in ZNCC traces of the main result for a delay range [-140,-130] fs. **b**, ZNCC traces taken in a main experimental geometry, without 3R-MoS_2 at 750 nm.

Finally, we demonstrate that holographic stabilization originates exclusively from the 3R-MoS_2 layer by modulating 750 nm light incident on the metasurface (see the experiment layout in Fig. 6c). This configuration reduces the hologram formation process to its delay-dependent interference aspect only. The resulting traces in Fig. 5b reveal that in the vicinity of zero delay ($\tau_D = 0 \pm 5$ fs), no plateau features are observed in either holographic channel. Instead, the correlation dynamics is driven by a $\sigma^{(\omega)} \propto \sin\varphi$ derived from the pump field amplitudes, see Eq. (2).

Dicussion

In this work, we have identified and exploited a nonlinear symmetry-protected circular polarization purification effect in second-harmonic generation from a thick 3R-MoS_2 crystal. We derived a general relation $|\sigma^{(2\omega)}| \geq |\sigma^{(\omega)}|$ showing that this bound is dictated solely by the C_{3v} symmetry of the $\chi^{(2)}$ tensor rather than by the specific pumping

scheme. For the delay-controlled excitation geometry used here, this purification manifests as stable plateaus of pure left- and right-handed circular polarization arising because the second-harmonic ellipticity vanishes quartically near circular pump polarization, in contrast to the pump's quadratic sensitivity. Combining this effect with a Pancharatnam-Berry phase metasurface, we demonstrated delay-dependent holographic switching between two channels with high fidelity (ZNCC ≈ 0.9) and channel transitions confined to below one femtosecond. We further showed that this switching behavior persists, with reduced but still robust contrast, over delay ranges as large as ± 140 fs confirming that the purification mechanism remains effective even under substantial pump ellipticity degradation. Control measurements without the 3R-MoS_2 layer confirmed that this polarization stabilization originates exclusively from the nonlinear medium and is absent in a purely interferometric (linear) analog of the setup.

A natural extension of these ideas is the development of an integrated platform combining the properties of the nonlinear crystal and the metasurface within a single device. The most straightforward route is direct transfer of a monolayer or a thick 3R-TMD flake onto the metasurface itself. This requires accounting for the crystal's high refractive index and its optical anisotropy. For a thick flake, the metasurface design may consequently depend on the crystal thickness - a constraint that, however, does not appear prohibitive. Monolayer transfer, in contrast, would require no modification of existing metasurface designs, though at the cost of markedly lower SHG efficiency.

Another promising direction is to embed the circular polarization purification effect directly within a 3R-TMD-based nonlinear metasurface. Preserving the effect in this geometry requires that the combined symmetry of the material and the metasurface unit cell be maintained - a condition achievable, for instance, with a triangular unit cell. Under these conditions, the purification effect would endow such a nonlinear metasurface with an additional degree of functionality.

Together, these results establish 3R-TMDs as an efficient nonlinear platform for generating robust, delay-encoded circular polarization states on ultrashort timescales, and demonstrate their direct applicability to sub-femtosecond-scale wavefront and hologram control via phase-modulating metasurfaces. Beyond hologram switching, the intrinsic robustness of this symmetry-protected purification against pump ellipticity and delay fluctuations suggests a broader route toward polarization-encoded information processing, where the tensor symmetry of the nonlinear medium rather than active feedback or filtering provides passive, built-in protection of the encoded polarization state.

Methods

Optical characterization methods

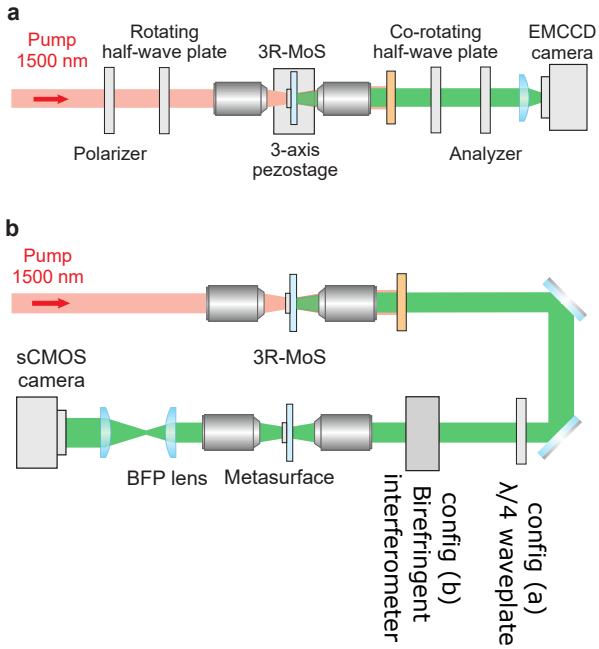


Fig. 6 Layouts of auxiliary experimental setups. **a** SHG-mapping and polarization characterization setup. **b** PB-phase metasurface hologram imaging setup.

In the SHG mapping setup (see Fig. 6a), fundamental light at a wavelength of 1500 nm was focused onto the 3R-TMD crystal with a Mitutoyo NIR x10 objective lens. The generated SHG signal was collected using a Mitutoyo VIS x20 objective lens and projected onto an Andor iXon3 EMCCD camera. For all other measurements, the same combination of objective lenses was used. The sample was mounted on a high-precision three-axis stage (assembled using three Newport M-VP-25XL stages), which, together with the camera, was controlled via custom automated software. Spatial SHG mapping across the sample area was performed by defining a two-dimensional grid of the motorized stage in-plane positions and recording the corresponding SHG signal at each point.

Polarization-resolved SHG measurements can be performed by co-rotating a polarizer and an analyzer by the same angle. In practice, however, this is not feasible, since the pump itself is linearly polarized, so rotating the polarizer relative to this fixed polarization would suppress the transmitted pump. We therefore use an equivalent scheme, in which half-wave plates, rotated synchronously by the same angle and likewise controlled by custom software, are placed after the polarizer and before the analyzer.

Pre-characterization of the metasurface, together with an additional experiment probing hologram formation driven directly by an interferometrically modulated second harmonic, was carried out on the same experimental platform as the main measurement (Fig. 6b). The main difference here that the interferometer is now placed after 3R-MoS_2 crystal. As before, the fundamental beam at 1500 nm generated the second harmonic in the 3R-MoS_2 crystal. While a separate 750 nm source without TMD material would, in principle, suffice for metasurface characterization, this configuration ensures that the SH power incident on the metasurface matches that of the main experiment. The setup was operated in two configurations. In the first (configuration (a)), the interferometer was removed and a quarter-wave plate was inserted in the pump channel illuminating the metasurface; depending on its orientation, holograms were recorded under RCP and LCP light at 750 nm. In the second configuration (configuration (b)), the quarter-wave plate was removed and the interferometer reinstated, so that the 750 nm beam itself was routed through the interferometer and delayed. In this configuration, the field incident on the metasurface carries an unpurified, pump-like DOCP modulation $\sigma^{(\omega)} = \sin\varphi$ (Eq. (2)), which directly drives the correlation trace shown in Fig. 5b.

3R-MoS_2 sample fabrication

Our 3R-MoS_2 samples were created by mechanically exfoliating flakes from a commercially acquired bulk crystal (HQ Graphene) using the scotch tape method and transferred onto a fused silica glass substrate in a polydimethylsiloxane (Gel-Pak, PF-30-X4)-based stamping process.

Data availability

The raw data and scripts used to compute the ZNCC values are available at Zenodo open database via a reference. An animation of all experimentally recorded holographic images at their corresponding time delays, together with the detailed mathematical derivations, is provided in the Supplementary Information, available at [URL].

Acknowledgments

This work was funded by CRC 1375 NOA and IRTG 2675 Meta-Active. The work was supported by the Free State of Thuringia and the European Social Fund Plus. The authors thank Giancarlo Soavi and Sebastian Klimmer for discussions on the measurement methodology. The authors are deeply grateful to Ivan Toftul for valuable comments and discussions throughout this work.

Author contributions

D.P. and I.S. conceived the idea. D.P. carried out the optical experiments. B.L. fabricated 3R-MoS_2 sample. D.C. fabricated optical metasurfaces. S.H.L carried out the numerical calculations. D.P. and S.H.L. investigated theoretical models. D.P. wrote the manuscript with the help of all authors.

Competing interests

The authors declare no competing interests.

Supplementary information

Second harmonic DOCP stabilization

In the main text, the DOCP of the pump and of the second harmonic were obtained as

$$\sigma^{(\omega)} = \sin\varphi, \qquad \sigma^{(2\omega)} = -\frac{2\sin\varphi}{1+\sin^2\varphi}. \tag{6}$$

For $\varphi = \pi/2$, which corresponds to the right-handed circular polarization of the excitation, $\sigma^{(2\omega)} = -1$. As expected [16, 25], the polarization of the second harmonic is flipped to left-handed. We now let the pump deviate slightly from pure circular polarization, $\varphi = \pi/2 + \delta$ with $|\delta| \ll 1$. This corresponds to a right-circularly polarized pump with a small ellipticity, $\sigma^{(\omega)} \approx 1 - \delta^2/2$. The second harmonic DOCP reads as:

$$\sigma^{(2\omega)} \approx -1 + \frac{\delta^4}{8}, \tag{7}$$

where the linear, quadratic and cubic terms of the expansion vanish. The pump loses circularity quadratically in δ, whereas the second harmonic loses it only quartically; i.e., the second harmonic is more circularly pure than the pump that generates it. This produces a stationary plateau in $\sigma^{(2\omega)}$ at its extreme value of -1, a purely left-handed second harmonic held over a finite range of delay (see upper inset in Fig. 1). The mirror point $\varphi = -\pi/2 + \delta$ produces a right-handed one.

Derivation of the general circular polarization purification relation

Equation (4) of the main text could naively be obtained by substituting $\sigma^{(\omega)} = \sin\varphi$ directly into the expression for $\sigma^{(2\omega)}$, though such a derivation would not be fully rigorous. The DOCP of the second harmonic is, first and foremost, a function of the second-harmonic fields themselves, and this does not automatically guarantee that it can be expressed explicitly in terms of the pump DOCP. Nevertheless, this relation can indeed be established. The degree of circular polarization of the second harmonic is defined on its own fields:

$$\sigma^{(2\omega)} = \frac{2\,\mathrm{Im}\left\{\left(E_x^{(2\omega)}\right)^* E_y^{(2\omega)}\right\}}{\left|E_x^{(2\omega)}\right|^2 + \left|E_y^{(2\omega)}\right|^2}, \tag{8}$$

Substituting the second-harmonic fields generated by a C_{3v} medium,

$$E_x^{(2\omega)} \propto 2E_xE_y, \qquad E_y^{(2\omega)} \propto E_x^2 - E_y^2 \tag{9}$$

into (8) yields $\sigma^{(2\omega)}$ as a function of the pump components. We evaluate it for arbitrary complex E_x and E_y, i.e. without assuming balanced amplitudes or any particular excitation scheme. We introduce the shorthand notation:

$$I \equiv \mathrm{Im}\{E_x^* E_y\}, \qquad |\mathbf{E}|^2 = |E_x|^2 + |E_y|^2, \tag{10}$$

so that $\sigma^{(\omega)} = 2I/|\mathbf{E}|^2$. Using $\mathrm{Im}\{E_x E_y^*\} = -I$, the numerator of (8) reads:

$$\begin{aligned} 2\,\mathrm{Im}\left\{(2E_xE_y)^*\left(E_x^2 - E_y^2\right)\right\} &= 4\,\mathrm{Im}\left\{|E_x|^2 E_x E_y^* - |E_y|^2 E_x^* E_y\right\} = \\ &= -4I\,|\mathbf{E}|^2 = -2\sigma^{(\omega)}|\mathbf{E}|^4. \end{aligned} \tag{11}$$

The denominator of (8) is the total second-harmonic intensity:

$$\left|E_x^{(2\omega)}\right|^2 + \left|E_y^{(2\omega)}\right|^2 = |2E_xE_y|^2 + \left|E_x^2 - E_y^2\right|^2 \tag{12}$$

The first term is immediate, $|2E_xE_y|^2 = 4|E_x|^2|E_y|^2$. For the second, using[1] $\mathrm{Re}\left\{(E_x^*E_y)^2\right\} = (\mathrm{Re}\,\{E_x^*E_y\})^2 - (\mathrm{Im}\,\{E_x^*E_y\})^2 = |E_x|^2|E_y|^2 - 2I^2$,

$$\left|E_x^2 - E_y^2\right|^2 = |E_x|^4 + |E_y|^4 - 2\,\mathrm{Re}\left\{(E_x^*E_y)^2\right\} = \left(|E_x|^2 - |E_y|^2\right)^2 + 4I^2, \tag{13}$$

so that

$$4|E_x|^2|E_y|^2 + \left(|E_x|^2 - |E_y|^2\right)^2 + 4I^2 = |\mathbf{E}|^4 + 4I^2 = |\mathbf{E}|^4\left[1 + \left(\sigma^{(\omega)}\right)^2\right], \tag{14}$$

Dividing (11) by (14), the factors $|\mathbf{E}|^4$ cancel and the pump components combine into the SHG DOCP alone:

$$\sigma^{(2\omega)} = -\frac{2\,\sigma^{(\omega)}}{1 + \left(\sigma^{(\omega)}\right)^2} \tag{15}$$

Since $2/\left[1 + \left(\sigma^{(\omega)}\right)^2\right] \in [1, 2]$ for $\sigma^{(\omega)} \in [-1, 1]$, Eq. (15) implies

$$\left|\sigma^{(2\omega)}\right| \geq \left|\sigma^{(\omega)}\right|, \tag{16}$$

with equality only at $\sigma^{(\omega)} = 0$ and $\sigma^{(\omega)} = \pm 1$. The second harmonic is therefore never less circularly pure than the pump that generates it. For the delay-controlled excitation scheme, this relation reduces exactly to the expression given in Eq. (3) of the main text. The two ingredients of Eq. 3 of the main text are worth keeping apart. The transfer relation (15) belongs to the medium. The specific dependence

$$\sigma^{(\omega)} = \sin\varphi, \qquad \varphi = \omega_0\tau_D, \tag{17}$$

[1] For a complex z, $\mathrm{Re}\left\{z^2\right\} = (\mathrm{Re}\,z)^2 - (\mathrm{Im}\,z)^2 = |z|^2 - 2\,(\mathrm{Im}\,z)^2$.

belongs to the excitation scheme and holds only for two equal-amplitude, orthogonally polarized monochromatic components. Should the pump be elliptically polarized, amplitude-imbalanced, or delayed by other means, (17) changes while (15) does not.

Design method of the holographic phase mask

The holographic phase masks were obtained using the method outlined in Chapter 7.3 of [31], which assumed plane-wave incidence and periodic boundary conditions. Our holographic phase masks consist of 150×150 phase elements. The target holographic projection images are also 150×150 pixels accordingly. To limit the back-focal plane holographic projection of the "META" and "FAST" logos within a small numerical aperture and to avoid their overlap with the bright specular transmission of the incident beam and diffraction orders of the metasurface, the logos were placed in small regions (60×19 pixels and 44×19 pixels, respectively) above the center of the target image.

Decomposition of the second-harmonic intensity into circular components

For comparison with the experimentally measured hologram correlations, it is natural to express the second-harmonic field in the circular basis. The circular basis vectors are defined as [39]

$$\hat{\boldsymbol{e}}_R = \frac{1}{\sqrt{2}}\left(\hat{\boldsymbol{x}} - i\hat{\boldsymbol{y}}\right), \qquad \hat{\boldsymbol{e}}_L = \frac{1}{\sqrt{2}}\left(\hat{\boldsymbol{x}} + i\hat{\boldsymbol{y}}\right), \tag{18}$$

so that the second-harmonic field, Eq. (3), can be written as

$$\mathbf{E}^{(2\omega)} \propto (1 - \sin\varphi)\,\hat{\boldsymbol{e}}_R + (1 + \sin\varphi)\,\hat{\boldsymbol{e}}_L = C_R\,\hat{\boldsymbol{e}}_R + C_L\,\hat{\boldsymbol{e}}_L. \tag{19}$$

The squared moduli of the expansion coefficients,

$$|C_R|^2 = (1 - \sin\varphi)^2, \qquad |C_L|^2 = (1 + \sin\varphi)^2, \tag{20}$$

quantify the contribution of the RCP and LCP components of the second harmonic to the hologram generation as a function of delay. However, the total second-harmonic intensity itself also depends on delay, so these quantities must be normalized before comparison with the ZNCC in the experiment:

$$SH_R = \frac{|C_R|^2}{|\mathbf{E}^{(2\omega)}|^2}, \qquad SH_L = \frac{|C_L|^2}{|\mathbf{E}^{(2\omega)}|^2}. \tag{21}$$

References

[1] Azimi, A., Barrier, J., Barreda, A., Bauer, T., Bouzari, F., Brokkelkamp, A., Mongeot, F., Parsons, T., Christianen, P., Conesa-Boj, S., *et al.*: Photonics in

flatland: challenges and opportunities for nanophotonics with 2d semiconductors. npj Nanophotonics **2**(1), 44 (2025)

[2] Wang, G., Chernikov, A., Glazov, M.M., Heinz, T.F., Marie, X., Amand, T., Urbaszek, B.: Colloquium: Excitons in atomically thin transition metal dichalcogenides. Reviews of Modern Physics **90**(2), 021001 (2018)

[3] Kumar, N., Najmaei, S., Cui, Q., Ceballos, F., Ajayan, P.M., Lou, J., Zhao, H.: Second harmonic microscopy of monolayer mos 2. Physical Review B—Condensed Matter and Materials Physics **87**(16), 161403 (2013)

[4] Abajo, F.J.G., Basov, D.N., Koppens, F.H., Orsini, L., Ceccanti, M., Castilla, S., Cavicchi, L., Polini, M., Gonçalves, P.A.D., Costa, A.T., *et al.*: Roadmap for photonics with 2d materials. ACS photonics **12**(8), 3961–4095 (2025)

[5] Yao, K., Yanev, E., Chuang, H.-J., Rosenberger, M.R., Xu, X., Darlington, T., McCreary, K.M., Hanbicki, A.T., Watanabe, K., Taniguchi, T., *et al.*: Continuous wave sum frequency generation and imaging of monolayer and heterobilayer two-dimensional semiconductors. ACS nano **14**(1), 708–714 (2019)

[6] Autere, A., Jussila, H., Dai, Y., Wang, Y., Lipsanen, H., Sun, Z.: Nonlinear optics with 2d layered materials. Advanced Materials **30**(24), 1705963 (2018)

[7] Wen, X., Gong, Z., Li, D.: Nonlinear optics of two-dimensional transition metal dichalcogenides. InfoMat **1**(3), 317–337 (2019)

[8] Xu, X., Trovatello, C., Mooshammer, F., Shao, Y., Zhang, S., Yao, K., Basov, D.N., Cerullo, G., Schuck, P.J.: Towards compact phase-matched and waveguided nonlinear optics in atomically layered semiconductors. Nature Photonics **16**(10), 698–706 (2022)

[9] Weissflog, M.A., Fedotova, A., Tang, Y., Santos, E.A., Laudert, B., Shinde, S., Abtahi, F., Afsharnia, M., Pérez Pérez, I., Ritter, S., *et al.*: A tunable transition metal dichalcogenide entangled photon-pair source. Nature Communications **15**(1), 7600 (2024)

[10] Peng, Z.H., Cotrufo, M., Xu, D., Mann, S.A., Qiu, S., Basov, D., Delor, M., Alú, A., Schuck, P.J., Trovatello, C.: 3r-stacked transition metal dichalcogenide non-local metasurface for efficient second-harmonic generation. Nature Photonics **19**(12), 1376–1384 (2025)

[11] Wagoner, G., Persans, P., Van Wagenen, E., Korenowski, G.: Second-harmonic generation in molybdenum disulfide. Journal of the Optical Society of America B **15**(3), 1017–1021 (1998)

[12] Zograf, G., Polyakov, A.Y., Bancerek, M., Antosiewicz, T.J., Küçüköz, B., Shegai, T.O.: Combining ultrahigh index with exceptional nonlinearity in resonant

transition metal dichalcogenide nanodisks. Nature Photonics **18**(7), 751–757 (2024)

[13] Liu, Y., Zhao, Y., Ye, F., Liang, L., Zhao, T., Guan, Z., Fu, J., Wang, J.-P., Xie, X., Lu, R., *et al.*: Determining the dipole orientation of second harmonic generation in 3r-mos2 for enhanced nonlinear susceptibility. ACS nano **19**(35), 31882–31893 (2025)

[14] Zograf, G., Küçüköz, B., Polyakov, A.Y., Yankovich, A.B., Ranjan, A., Bancerek, M., Agrawal, A.V., Olsson, E., Wieczorek, W., Antosiewicz, T.J., *et al.*: Ultrathin 3r-mos2 metasurfaces with atomically precise edges for efficient nonlinear nanophotonics. Communications Physics **8**(1), 271 (2025)

[15] Seidt, L., Weber, T., Seredin, A.A., Possmayer, T., Savelev, R., Petrov, M.I., Maier, S.A., Tittl, A., Menezes, L.d.S., Sortino, L.: Ultrafast all-optical switching in nonlinear 3r-mos2 van der waals metasurfaces. npj Nanophotonics **2**(1), 37 (2025)

[16] Klimmer, S., Ghaebi, O., Gan, Z., George, A., Turchanin, A., Cerullo, G., Soavi, G.: All-optical polarization and amplitude modulation of second-harmonic generation in atomically thin semiconductors. Nature Photonics **15**(11), 837–842 (2021)

[17] Sinelnik, A., Lam, S.H., Coviello, F., Klimmer, S., Della Valle, G., Choi, D.-Y., Pertsch, T., Soavi, G., Staude, I.: Ultrafast all-optical second harmonic wavefront shaping. Nature Communications **15**(1), 2507 (2024)

[18] Wang, H., Hu, Z., Deng, J., Zhang, X., Chen, J., Li, K., Li, G.: All-optical ultrafast polarization switching with nonlinear plasmonic metasurfaces. Science Advances **10**(8), 3882 (2024)

[19] Boyd, R.W., Gaeta, A.L., Giese, E.: Nonlinear optics. In: Springer Handbook of Atomic, Molecular, and Optical Physics, pp. 1097–1110. Springer, ??? (2008)

[20] Butcher, P.N., Cotter, D.: The Elements of Nonlinear Optics. Cambridge university press, ??? (1990)

[21] Malard, L.M., Alencar, T.V., Barboza, A.P.M., Mak, K.F., De Paula, A.M.: Observation of intense second harmonic generation from mos 2 atomic crystals. Physical Review B—Condensed Matter and Materials Physics **87**(20), 201401 (2013)

[22] Jackson, J.D., Jackson, J.D.: Classical electrodynamics (1962)

[23] Born, M., Wolf, E., *et al.*: Principles of Optics vol. 6. Pergamon press Oxford, ??? (1964)

[24] Mok, J., Lee, H.-I.: Degrees of circular polarization for the electromagnetic waves induced by electric point dipoles. Optics Continuum **1**(4), 772–785 (2022)

[25] Molina, L.V., Fedorova, Z., Barreda, A., Weissflog, M., Morales, R.C., Han, S.H., Romashkina, A., George, A., Das, S., Bucher, T., *et al.*: Role of coherence in polarization response of hybrid monolayer mos2-gold nanoparticle systems. Advanced Physics Research **5**(1), 00104 (2026)

[26] Shi, J., Yu, P., Liu, F., He, P., Wang, R., Qin, L., Zhou, J., Li, X., Zhou, J., Sui, X., *et al.*: 3r mos2 with broken inversion symmetry: a promising ultrathin nonlinear optical device. Advanced Materials **29**(30), 1701486 (2017)

[27] Munkhbat, B., Wróbel, P., Antosiewicz, T.J., Shegai, T.O.: Optical constants of several multilayer transition metal dichalcogenides measured by spectroscopic ellipsometry in the 300–1700 nm range: high index, anisotropy, and hyperbolicity. ACS photonics **9**(7), 2398 (2022)

[28] Li, Y., Rao, Y., Mak, K.F., You, Y., Wang, S., Dean, C.R., Heinz, T.F.: Probing symmetry properties of few-layer mos2 and h-bn by optical second-harmonic generation. Nano letters **13**(7), 3329–3333 (2013)

[29] Torchinsky, D.H., Chu, H., Qi, T., Cao, G., Hsieh, D.: A low temperature nonlinear optical rotational anisotropy spectrometer for the determination of crystallographic and electronic symmetries. Review of Scientific Instruments **85**(8) (2014)

[30] Wyrowski, F., Bryngdahl, O.: Iterative fourier-transform algorithm applied to computer holography. Journal of the Optical Society of America A **5**(7), 1058–1065 (1988) https://doi.org/JOSAA.5.001058

[31] Poon, T.-C., Liu, J.-P.: Introduction to Modern Digital Holography: with MATLAB. Cambridge University Press, ??? (2014). https://doi.org/CBO9781139061346

[32] Arbabi, A., Horie, Y., Bagheri, M., Faraon, A.: Dielectric metasurfaces for complete control of phase and polarization with subwavelength spatial resolution and high transmission. Nature nanotechnology **10**(11), 937–943 (2015) https://doi.org/nnano.2015.186

[33] Novotny, L., Hecht, B., *et al.*: Principles of Nano-optics vol. 2. Cambridge university press New York, US, ??? (2006)

[34] Pan, B., Xie, H., Wang, Z.: Equivalence of digital image correlation criteria for pattern matching. Applied optics **49**(28), 5501–5509 (2010)

[35] Tanaka, K.: Mie-resonant silicon metasurfaces for advanced light shaping. PhD thesis, Verlagsname nicht ermittelbar (2026)

[36] Pan, B.: Reliability-guided digital image correlation for image deformation measurement. Applied optics **48**(8), 1535–1542 (2009)

[37] Atkinson, D., Becker, T.H.: Stereo digital image correlation in matlab. Applied Sciences **11**(11), 4904 (2021)

[38] Wang, J., Li, G.: Study on bridge displacement monitoring algorithms based on multi-targets tracking. Future Internet **12**(1), 9 (2020)

[39] Frizyuk, K., Menshikov, E., Spera, M.: Geometric phases and holonomy in structured optical fields. arXiv preprint arXiv:2602.05427 (2026)

Supplementary Files

This is a list of supplementary files associated with this preprint. Click to download.

- ZNCCanimation.mp4